molecules

MDPI

Article

Synthesis and Magnetic and Optical Properties of Novel Fe@ZSM-5 Composites

Irina A. Zvereva [1], Denis A. Pankratov [2,3], Elena G. Zemtsova [1], Vladimir K. Kudymov [1], Azamat Samadov [1], Sergey A. Kurnosenko [1], Sergey O. Kirichenko [4], Marina G. Shelyapina [5,*] and Vitalii Petranovskii [6]

1 Institute of Chemistry, Saint Petersburg State University, 7/9 Universitetskaya Embankment, Saint Petersburg 199034, Russia; irina.zvereva@spbu.ru (I.A.Z.); e.zemtsova@spbu.ru (E.G.Z.); v.k.kudymov@spbu.ru (V.K.K.); st088712@student.spbu.ru (A.S.); s.kurnosenko@spbu.ru (S.A.K.)
2 Department of Chemistry, Lomonosov Moscow State University, Leninskie Gory 1/3, Moscow 119991, Russia; pankratov@radio.chem.msu.ru
3 Moscow Center for Advanced Studies, 20, Kulakova Str., Moscow 123592, Russia
4 Centre for Innovative Technologies of Composite Nanomaterials, Saint Petersburg State University, 7/9 Universitetskaya Embankment, Saint Petersburg 199034, Russia; sergey.kirichenko@spbu.ru
5 Department of Nuclear Physics Research Methods, Faculty of Physics, Saint Petersburg State University, 7/9 Universitetskaya Embankment, Saint Petersburg 199034, Russia
6 Centro de Nanociencias y Nanotecnología, Universidad Nacional Autónoma de México, Ensenada 22800, BC, Mexico; vitalii@ens.cnyn.unam.mx
* Correspondence: marina.shelyapina@spbu.ru

Abstract

Alkaline treatment in 0.2 and 0.4 M NaOH solutions successfully generated controlled mesoporosity into ZSM-5 (Zeolite Socony Mobil-5) zeolite, resulting in average mesopore diameters of approximately 15 and 25 nm, respectively, while preserving the crystalline structure of the zeolite framework. Parent ZSM-5 and its mesoporous derivatives obtained by desilication were used to prepare (Fe species)@(zeolite matrix) composites. The synthesis was carried out by co-precipitating Fe^{2+}/Fe^{3+} ions onto both parent and desilicated ZSM-5 matrices under oxygen-free conditions. Comprehensive characterization by X-ray diffraction, scanning electron microscopy, N_2 adsorption, vibrating-sample magnetometry, ^{57}Fe Mössbauer spectroscopy, and diffuse reflectance UV–Vis spectroscopy revealed that the degree of introduced mesoporosity dramatically influences the size, dispersion, phase composition, and oxidation state of the iron-containing nanospecies. On purely microporous ZSM-5, relatively large (~15 nm) partially oxidized magnetite nanoparticles are formed predominantly on the external surface, exhibiting superparamagnetism at room temperature (M_s = 11 emu/g) and a band gap of 2.12 eV. Increasing mesoporosity leads to progressively smaller and more highly dispersed iron(III) oxo/hydroxo clusters with significantly lower blocking temperatures and reduced magnetization (down to 0.7 emu/g for Fe@ZSM-5_0.4). All composites display strong visible-light absorption confirming their potential as magnetically separable visible-light-driven photocatalysts for environmental remediation.

Keywords: zeolite; ZSM-5; mesoporosity; magnetite; composite; Mössbauer spectroscopy; vibrating-sample magnetometry; UV-Vis spectroscopy

Check for updates

Academic Editor: Wenfu Yan

Received: 1 December 2025
Revised: 18 December 2025
Accepted: 23 December 2025
Published: 25 December 2025

Copyright: © 2025 by the authors. Licensee MDPI, Basel, Switzerland. This article is an open access article distributed under the terms and conditions of the Creative Commons Attribution (CC BY) license.

1. Introduction

Zeolites have been among the most important heterogeneous catalysts [1,2] and adsorbents [3,4] for several decades due to their ordered microporous structure (pore diameters of 0.3–1.2 nm) [5], high specific surface area (typically 300–700 m^2/g) [6], excellent thermal

and chemical stability [7], and the ability to finely tune their Brønsted and Lewis acidity [8,9], as well as their cation composition [10,11]. In recent years, increasing attention has been devoted to their application in photocatalytic purification of water and air [12–14], where zeolites serve either as supports for photoactive species or as intrinsic wide-band-gap semiconductor materials [14–17]. However, pristine zeolite frameworks possess a large band gap (E_g > 3.0–3.8 eV), which restricts their photoactivity to the ultraviolet region of the spectrum—a region that constitutes less than 5% of the solar radiation reaching the Earth's surface [18]. This severely limits their practical utilization in solar-driven photocatalysis and increases energy consumption when artificial UV sources are required [12].

A widely adopted strategy to overcome this limitation involves modification of zeolites with photoactive transition metals and their oxides, which narrow the effective band-gap, extend light absorption into the visible region, and create heterojunctions that facilitate efficient separation of photogenerated electrons and holes [14,19–21]. Among the various candidates, iron oxides (in particular magnetite Fe_3O_4, maghemite γ-Fe_2O_3, and hematite α-Fe_2O_3) attract the greatest attention due to their earth abundance, low cost, environmental compatibility, high photochemical stability, and suitable electronic band-edge positions [12,22,23]. Magnetite is especially attractive because of its relatively narrow band gap of about 2.2–2.4 eV, which enables strong absorption of visible light up to ~600 nm and facilitates multielectron charge-transfer processes [24]. Iron oxides are redox active [25,26]. Under both UV and visible irradiation, Fe_3O_4 efficiently generates highly reactive oxygen species, including hydroxyl radicals (•OH), superoxide anion radicals (O_2•$^-$), and singlet oxygen ($^1O_2$) [27].

A particularly important advantage of magnetite is its pronounced ferrimagnetic properties, with saturation magnetization of ~90–100 emu/g at room temperature [28]. This property allows rapid and nearly complete magnetic separation of catalyst nanoparticles from the treated aqueous suspensions using a simple external permanent magnet or a weak electromagnet. This addresses two critical technological challenges of heterogeneous photocatalysis—facile reuse of the catalyst and prevention of secondary contamination by metal-based nanoparticles [29–31].

Composites combining ZSM-5 zeolite with deposited or encapsulated magnetite nanoparticles (commonly denoted as Fe@ZSM-5 or Fe_3O_4@ZSM-5) exploit multiple synergistic effects: (i) the high adsorption capacity of the zeolite toward organic pollutants, which increases the local reactant concentration near the photoactive sites; (ii) high dispersion and firm anchoring of magnetite nanoparticles within the pores and on the external surface of the zeolite, suppressing their aggregation and leaching; (iii) the possibility of magnetic separation and multiple recycling without significant loss of activity; (iv) photoresponse, significantly extended into the visible spectral region. Altogether, these features make such materials highly promising heterogeneous photocatalysts for the degradation of a wide range of persistent organic pollutants, including phenols, chlorophenols, textile dyes (e.g., methylene blue, rhodamine B, Congo red), pharmaceutical residues, and pesticides in aqueous media [14,23,32–34].

The target properties of Fe@zeolite composites depend on both the characteristics of the zeolite matrix and the method used for the synthesis and introduction of iron species [23,35]. The most commonly employed techniques include wet impregnation [36,37], ion exchange [38–40] (including sonochemically assisted variants [41]), and hydrothermal synthesis [42,43].

Conventional 3D zeolites are classified as microporous materials, since the size of their voids (d) typically does not exceed 1 nm. Their highly ordered structures with precisely defined pores, whose diameters match the size of small molecules, endow crystalline zeolites with valuable shape- and size-selectivity. However, as a direct consequence of

these very advantages, the micropores impose significant diffusion limitations on the mass transfer of bulkier molecules.

The prospect of extending zeolite applications to new fields has prompted numerous attempts to synthesize mesoporous zeolitic materials that combine diffusion pathways on multiple length scales [44]. Consequently, in recent years growing interest has focused on zeolites with hierarchical porosity [6,45–53], i.e., zeolitic materials that integrate micro-, meso- and/or macropores. According to the IUPAC classification, porous materials are categorized as microporous (d < 2 nm), mesoporous (2 < d < 50 nm), and macroporous (d > 50 nm). The introduction of secondary (meso- and/or macro-) porosity is generally regarded as a strategy to enhance mass transfer and accelerate reaction kinetics [6,44,45,54,55]. However, it also influences the nature, dispersion, and phase composition of the supported iron species [40].

Thus, the design and comprehensive investigation of novel composites based on zeolite matrices with varying degrees of post-synthetically generated mesoporosity, modified with magnetite, represent a highly relevant and promising research direction. Such materials aim to create efficient, cost-effective, and technologically viable photocatalytic systems to address pressing environmental challenges in modern water purification.

In this contribution we report on the synthesis of novel Fe@ZSM-5 magnetic composites and their comprehensive study by complementary methods providing access to structural, textural, magnetic and optic properties of systems with magnetic species dispersed on a zeolite support, focusing the attention on the role of mesoporosity of the support on the nature and phase composition of formed iron species.

2. Results and Discussion

2.1. XDR, Morphology and Elemental Analysis

According to the nomenclature accepted by the International Zeolite Association (IZA), ZSM-5 has the MFI framework type, which is a three-letter code system recommended by the IZA to identify different zeolite framework structures [5]. The X-ray diffraction (XRD) patterns as well as textural properties of the zeolite matrices used as supports for iron species were previously reported in Ref. [40]. It was shown that alkaline treatment (i) preserves the MFI framework structure, (ii) significantly enhances mesoporosity: the parent material is predominantly microporous, whereas in the treated samples mesopores dominate the total pore volume. The average mesopore diameters are approximately 15 and 23 nm for ZSM-5_0.2 and ZSM-5_0.4, respectively.

XRD patterns of the prepared composites are shown in Figure 1. All samples retain the characteristic reflections of the MFI structure. The patterns of Fe@ZSM-5 and Fe@ZSM-5_0.2 display additional diffraction peaks at 2θ = 30.4, 35.6, 43.1, 53.6 and 57.3°, which correspond to the (220), (311), (400), (422) and (511) planes of magnetite Fe_3O_4 (JCPDS # 00-065-0731) or maghemite γ-Fe_2O_3 (JCPDS # 84–1595). These two phases are difficult to distinguish solely by XRD due to their nearly identical patterns. In contrast, sample Fe@ZSM-5_0.4, prepared using the zeolite matrix subjected to more severe alkaline treatment, exhibits a broad amorphous halo in the 2θ range of 20–35° (typical of hierarchical zeolites [51,56]) and no discernible reflections attributable to Fe_3O_4.

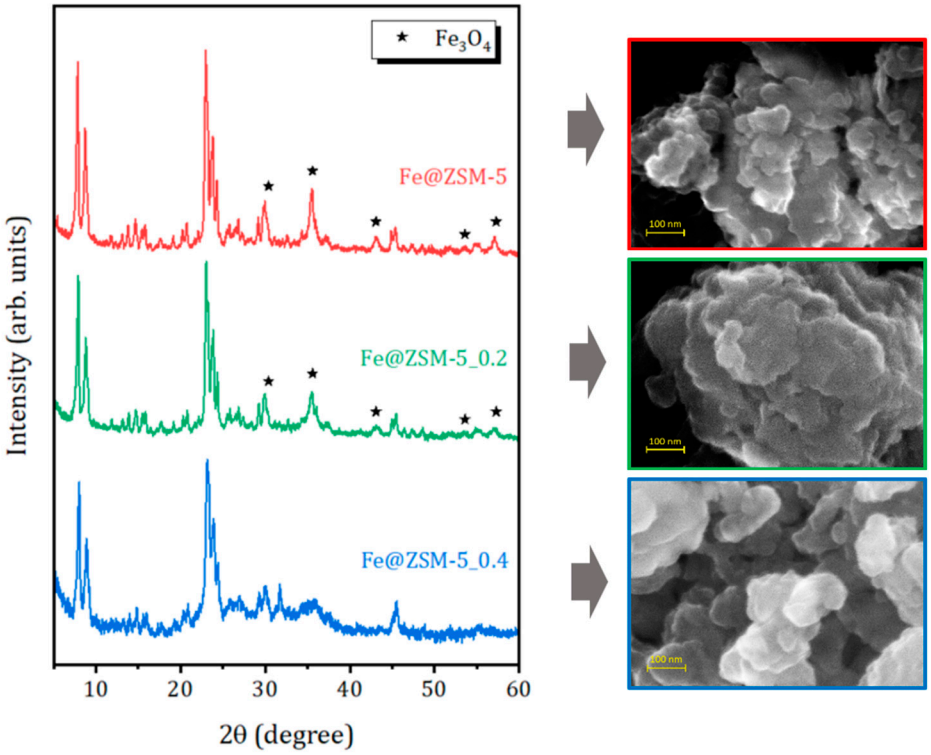


Figure 1. XRD patterns (on the **left**) and SEM images (on the **right**) of the studied composites. Solis symbols in the XDR patterns corresponds to iron Fe_3O_4 or γ-Fe_2O_3 oxide phases (see the text).

The morphology of the composite sample particles was studied by SEM. As shown in Figure 1 and Figure S1 (Supplementary Materials), all samples consist of plate-like individual crystals approximately 100–200 nm in size, aggregated into micron-sized particles. The introduction of iron species does not significantly alter the overall morphology of the zeolite particles (see Figure S1).

The chemical composition of the parent and desilicated zeolite matrices was reported previously [40] and listed in Table 1. The results confirm partial silicon leaching from the framework after alkaline treatment and concomitant substitution of the original $[NH_4]^+$ ions with Na^+.

Table 1. Chemical composition (atomic ratio) and Fe weight % for the studied samples as determined from EDXRF.

Sample	Si/Al	Fe/Al	Fe (wt%)
ZSM-5 *	10.15		
ZSM-5_0.2 *	7.77		
ZSM-5_0.4 *	4.96		
Fe@ZSM-5	11.1	11.1	26.7
Fe@ZSM-5_0.2	7.1	5.9	22.6
Fe@ZSM-5_0.4	6.7	11.3	34.9

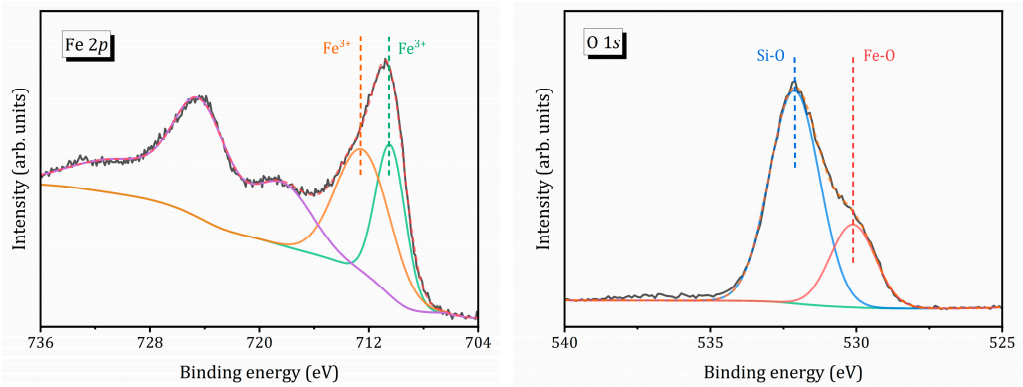
* data from Ref. [40].

The elemental distribution mappings obtained by energy-dispersive X-ray (EDX) spectroscopy reveals a uniform distribution of elements in the Fe@zeolite composites, see Figure S2 in Supplementary Materials. The results of the elemental analysis are summarized in Table 1.Incorporation of iron increases the Si/Al ratio, likely due to partial replacement of framework Al^{3+} by Fe^{3+}. A substantial excess of Fe compared to Al confirm the formation of extra-framework iron-containing species, consistent with the XRD results (Figure 1). Notably, sample Fe@ZSM-5_0.4 exhibits the highest iron content, while shows no detectable

crystalline iron oxide reflections in XRD, suggesting that the iron oxide nanoparticles are either highly dispersed or smaller than ~5 nm (below the XRD detection limit).

2.2. Surface Chemical Environment Analysis

Figure 2 shows the Fe 2*p* and O 1*s* X-ray photoelectron spectroscopy (XPS) spectra of the Fe@ZSM-5_0.4 composite. The high-resolution Fe 2*p* (Figure 2a) displays main binding energy peaks at approximately 711 eV and 725 eV, corresponding Fe $2p_{3/2}$ and Fe $2p_{1/2}$, respectively [57,58]. A broad satellite peak appears at around 718 eV [58]. However, only the Fe $2p_{3/2}$ peak can be unambiguously deconvoluted into two Gaussian components at 710.5 eV and 712.6 eV, which can be assigned to Fe^{2+} and Fe^{3+} species, respectively. The Fe^{2+} fraction is calculated to be 40% in Fe@ZSM-5_0.4 (Table 2). Table 2 also shows that the Fe^{2+}/Fe^{3+} ratio on the composite surface, as determined by XPS, slightly increases with increasing mesoporosity of the zeolite support.



(**a**) (**b**)

Figure 2. XPS spectra of Fe 2*p* (**a**) and O 1*s* (**b**) of the Fe@ZSM-5_0.4 composite. Colored lines show the decomposition of the corresponding XPS peaks into two Gaussian lines.

Table 2. Fe 2*p* and O 1*s* XPS valence analysis results (total areas in %) of the Fe@zeolite composites; the corresponding binding energies (E_b) are provided.

Sample	Fe		O	
	Fe^{2+}	Fe^{3+}	O_{Fe}	O_Z
	E_b = 710.5 eV	E_b = 712.6 eV	E_b = 530.1 eV	E_b = 532.1 eV
Fe@ZSM-5	37	63	79	21
Fe@ZSM-5_0.2	39	61	75	25
Fe@ZSM-5_0.4	40	60	74	26

Figure 2b illustrates the O 1*s* XPS spectrum of Fe@ZSM-5_0.4, which can be fitted with two Gaussian peaks located at 532.1 eV and 530.1 eV. The latter peak is attributed to oxygen associated with oxidized iron species (O_{Fe}) [58], whereas the peak at 532.1 eV is related to zeolite framework oxygen (O_Z) [17]. As shown in Tables 1 and 2, with increasing mesoporosity of the zeolite support, the iron content increases; however, the relative contribution of O_{Fe} on the surface decreases. This observation suggests that iron species are preferentially formed inside the mesopores.

2.3. N_2 Adsorption/Desorption

The N_2 adsorption/desorption isotherms at 77 K for the samples before and after iron incorporation, as well as the pore size distribution evaluated using the BJH (Barrett, Joyner and Halenda) method, are shown in Figure 3. The surface area (S_{BET}) estimated by the

Brunauer–Emmett–Teller (BET) method, as well the BJH pore volume V_{BJH} are listed in Table 3. The textural properties of the zeolite matrices used as supports for iron species were analyzed in Ref. [40]; here, we have focused on the role of iron incorporation.

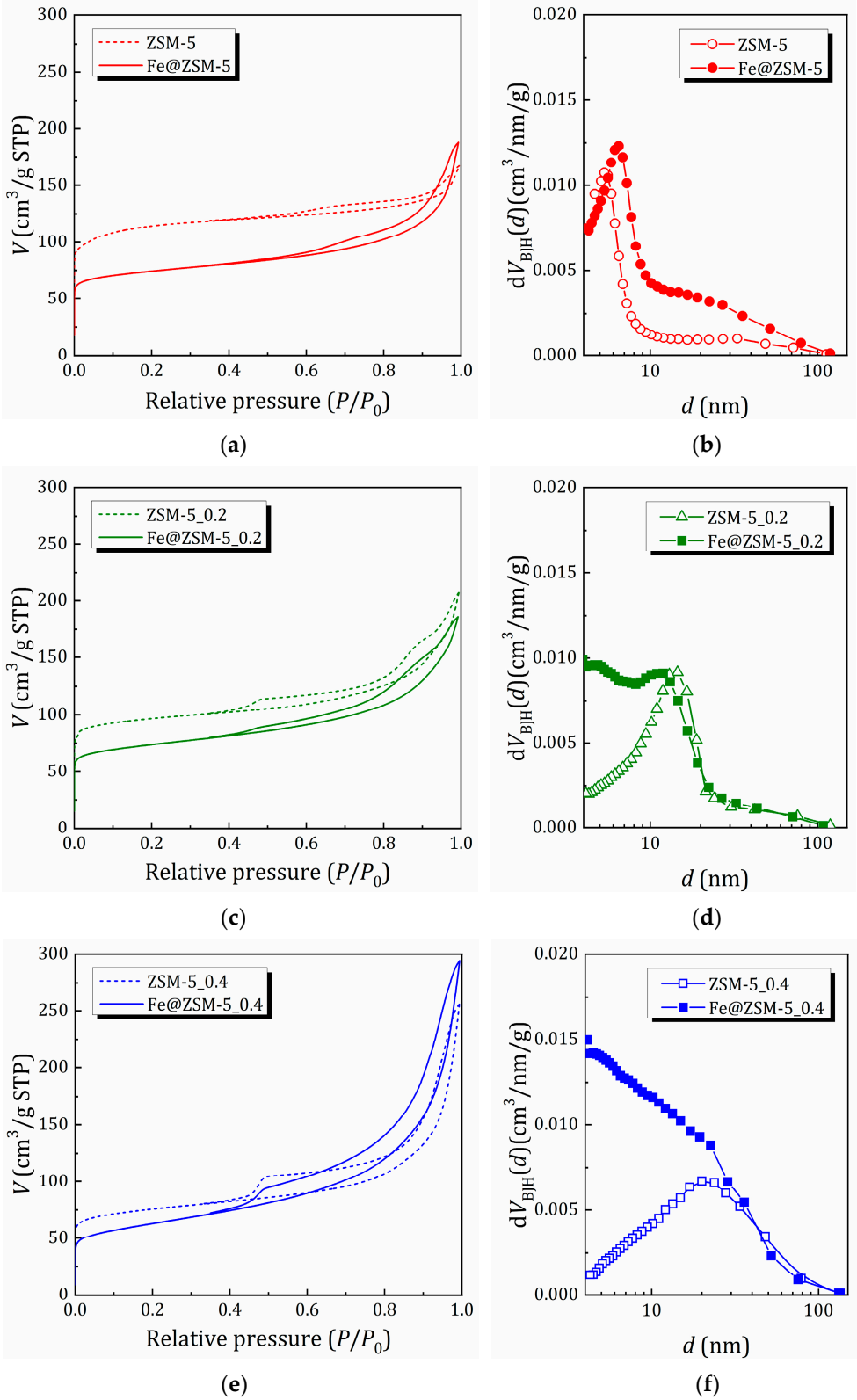


Figure 3. N_2 adsorption/desorption isotherms (**a**,**c**,**e**) and BJH pore size distribution (**b**,**d**,**f**) for the zeolite matrices before and after Fe incorporation.

Table 3. Textural properties of the samples before and after Fe incorporation.

Sample	S_{BET} (m^2/g)	V_{BJH} (cm^3/g)	V_{meso} (cm^3/g)	V_{micro} (cm^3/g)	V_{meso}/V_{micro}	D_{BJH} (nm)
ZSM-5	429	0.259	0.084	0.168	0.5	5
Fe@ZSM-5	281	0.291	0.190	0.109	1.7	6.5/15
ZSM-5_0.2	374	0.320	0.167	0.139	1.2	13
Fe@ZSM-5_0.2	277	0.287	0.184	0.108	1.7	>15
ZSM-5_0.2	284	0.395	0.262	0.111	2.4	23
Fe@ZSM-5_0.2	227	0.455	0.368	0.088	4.2	>23

For the ZSM-5 sample with high microporosity, the introduction of iron results in a significant decrease in surface area and micropore volume (V_{micro}); however, the total pore volume increases due to the appearance of larger mesopores. For other zeolite matrices pretreated in NaOH solution to introduce mesoporosity, iron incorporation also decreases the contribution of micropores to the surface area and pore volume, but to a lesser extent. It can also be noted that the ratio of mesopore volume (V_{meso}) to micropore volume (V_{micro}) increases (more dramatically for Fe@ZSM-5_0.4), which is due to the appearance of smaller mesopores. This allows us to suggest that (i) iron species block micropores and (ii) in the matrix with pre-introduced mesoporosity, these species are formed inside the mesopores, as also indicated by XPS analysis.

2.4. Magnetic Properties

The magnetic properties of the iron-containing composites—saturation magnetization (M_s) in the field range 0–1.8 kOe and coercive force (H_c)—were measured at room temperature using vibrating-sample magnetometry (VSM). Magnetization curves are shown in Figure 4, and key parameters are summarized in Table 4.

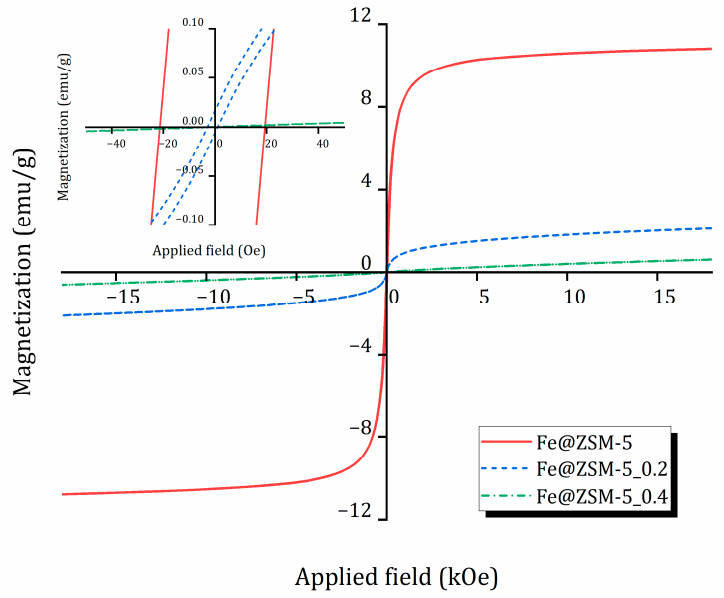


Figure 4. Magnetization hysteresis loop for studied composites at 300 K.

Table 4. Magnetic parameters of the studied composites (at 300 K).

Sample	M_s (emu/g)	H_c (Oe)
Fe@ZSM-5	11	23
Fe@ZSM-5_0.2	~2.5	4
Fe@ZSM-5_0.4	0.7	-

Sample Fe@ZSM-5 exhibits a hysteresis loop typical of superparamagnetic magnetite nanoparticles (Fe_3O_4). The magnitude of the coercive force is ≈ 23 Oe (see also Figure S3, Supplementary Materials). Its specific saturation magnetization is 11 emu/g, which is considerably lower than that of bulk Fe_3O_4 (~90–100 emu/g) but comparable with other reported Fe_3O_4/zeolite composites [59]. This reduction is primarily attributed to the relatively low magnetite content and nanoscale particle size.

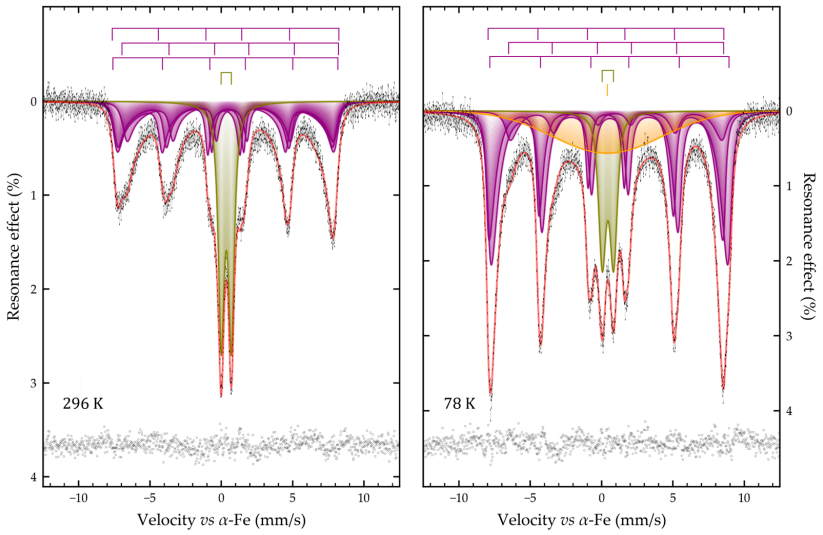
The magnetization curve of Fe@ZSM-5_0.2 reflects an intermediate behavior between paramagnetic and superparamagnetic states, suggesting the presence of additional iron-containing phases not detectable by XRD. Saturation is not reached even at 18 kOe. The estimated specific magnetization is approximately 2.5 emu/g, consistent with a decreased fraction of the magnetite phase, and the coercivity is about 4 Oe.

For the composite based on the most extensively desilicated matrix (Fe@ZSM-5_0.4), magnetic performance deteriorates sharply, which is attributed to partial oxidation of magnetite during synthesis or storage. This sample shows negligible superparamagnetic properties at room temperature (specific magnetization is only 0.7 emu/g) and a magnetization curve characteristic of paramagnetic materials.

2.5. Mössbauer Spectroscopy Studies

To identify the iron species in the obtained composites, ^{57}Fe Mössbauer spectroscopy was applied. The experimental spectra of the three samples differ markedly from one another and exhibit distinct temperature dependent behavior.

As shown in Figure 5, the Mössbauer spectra of Fe@ZSM-5 sample (iron species supported on microporous parent ZSM-5) recorded at 296 K and 78 K consist of broadened distorted Zeeman sextets superimposed on paramagnetic doublets. The sextet lines are significantly broadened toward the center of the spectrum, with broadening being more pronounced at room temperature (Figure 5a). Upon cooling to 78 K, the relative intensity of the magnetic sextets increases substantially: at 296 K their integrated area is approximately one-third that of the paramagnetic doublet, whereas at 78 K it becomes ~1.5 times larger (Figure 5b). This spectral profile and its temperature evolution are typical of nanoscale magnetite-based materials undergoing superparamagnetic relaxation [60,61].



(**a**) (**b**)

Figure 5. Mössbauer spectra of Fe@ZSM-5 sample obtained at 296 K (**a**) and 78 K (**b**). The size of the dashes corresponds to the error of the experimental points; the result of subtracting the model from the experimental spectrum is presented at the bottom of the figures.

The room-temperature spectrum was satisfactorily fitted by the superposition of one symmetrical quadrupole doublet and three magnetically split sextets (Figure 5a). If the doublet profile is described by the pseudo-Voigt function, then the sextets were set in accordance with the many-state superparamagnetic relaxation model. In this case, all three sextets were interconnected by relaxation parameters (Table 5). To satisfactorily describe the experimental spectra of the Fe@ZSM-5 sample at 78 K the model described above had to be supplemented with a singlet with a very large width (Figure 3b, Table 3). This component clearly corresponds to isolated poorly crystallized iron-containing clusters with weakly expressed ferromagnetism localized presumably in zeolite voids (microporous zeolites with MFI topology are characterized by channels in size of 5.1 Å × 5.5 Å and 5.3 Å × 5.6 Å) or on the external zeolite surface. Obviously, at room temperature, the contribution of this component is small, possibly due to a weak bond with the zeolite matrix.

Table 5. Hyperfine parameters of the Mössbauer spectra at different temperatures for the studied samples: δ is the isomer shift, ε {Δ = 2ε} is the quadrupole splitting, Γ_{exp} is the line width, H_{eff} is the hyperfine magnetic field, and S is the relative area of the subspectrum.

Sample	Temperature (K)	No.	δ (mm/s)	ε (mm/s)	Δ (mm/s)	Γ_{exp} (mm/s)	H_{eff} (kOe)	S (%)
Fe@ZSM-5	296(3)	1	0.250(21)	0.060(21)		0.300(23)	492.9(1.4)	27.82(13)
		2	0.683(20)	−0.054(13)		0.36(4)	470.7(1.9)	22.7(2.3)
		3	0.372(25)	−0.084(23)		0.26(3)	489.0(2.0)	23.9(2.3)
		4	0.36(1)		0.71(1)	0.50(1)		25.6(5)
	77.7(3)	1	0.33(1)	0.00(1)		0.36(1)	512.5(4)	25.2(1.5)
		2	0.968(29)	0.059(16)		0.70(8)	467.6(2.0)	8.1(1.0)
		3	0.57(1)	−0.01(1)		0.497(11)	520.5(4)	35.7(2.3)
		4	0.45(1)		0.79(1)	0.63(1)		12.2(1.1)
		5	0.41(4)			9.0(4)		19(5)
	5.000(3)	1	0.49(1)	0.08(1)		0.400(21)	540.7(7)	30(3)
		2	0.55(1)	−0.192(13)		0.464(29)	536.4(8)	22.6(2.7)
		3	0.41(1)	0.01(1)		0.520(23)	518.2(8)	37(4)
		4	0.74(4)	−0.059(16)		0.77(10)	488.3(2.3)	10.4(2.2)
Fe@ZSM-5_0.2	296(3)	1	0.36(1)		0.493(17)	0.27(6)		11(6)
		2	0.34(1)		0.764(22)	0.52(1)		89(6)
	77.7(3)	1	0.47(1)		0.63(3)	0.39(6)		13(8)
		2	0.44(1)		0.777(20)	0.599(26)		52(7)
		3	0.475(12)		1.30(29)	1.49(17)		35(9)
	5.000(3)	1	0.42(1)	−0.02(1)		0.435(17)	524.5(5)	45(4)
		2	0.74(1)	0.05(1)		0.362(20)	521.0(4)	22.9(2.4)
		3	0.38(1)	−0.07(1)		0.541(25)	506.3(1.1)	32(3)
Fe@ZSM-5_0.4	296(3)	1	0.35(1)		0.66(1)	0.40(20)		44(8)
		2	0.33(1)		0.86(3)	0.649(25)		56(8)
	77.7(3)	1	0.46(1)		0.56(3)	0.37(6)		26(17)
		2	0.45(1)		0.87(6)	0.549(14)		74(17)
	5.000(3)	1	0.40(1)	−0.03(1)		0.531(15)	514.8(5)	51(3)
		2	0.767(10)	0.04(1)		0.399(23)	509.2(4)	21.4(2.5)
		3	0.350(11)	−0.05(1)		0.548(27)	492.4(1.0)	27.3(2.7)

The obtained hyperfine parameters of the three sextets make it possible to attribute the materials to partially oxidized magnetite. Its composition can be expressed by the formula $Fe_{3-\delta}O_4$ (δ > 0). The sextets can be attributed to Fe^{3+} iron ions in three crystallographic positions of the spinel structure $(Fe^{3+})_{Td}(Fe^{2+}{}_{1-3\delta}Fe^{3+}{}_{1+2\delta}\#_{\delta})_{Oh}O_4$, where δ is the non-

stoichiometry parameter of magnetite [62], # is a vacancy in the O_h-sites [63,64]. The areas of these subspectra can be related by the following expression:

$$S_{T_d} = \frac{f\prime_{T_d}}{f\prime_{O_h}} \frac{\Sigma S_{O_h}}{(2-\delta)}, \quad (1)$$

where S_{T_d} is the relative area of a sextet with a lower isomeric shift (Table 5, subspectrum 1) corresponding to Fe^{3+} ions in tetrahedral positions of the spinel structure, ΣS_{O_h} is the sum of the relative areas of sextets with a higher isomeric shift (Table 5, subspectra 2 and 3) from Fe^{2+} and Fe^{3+} ions in octahedral positions of the spinel structure [65], $f\prime_{T_d}$ and $f\prime_{O_h}$ are the probabilities of the Mössbauer effect (recoilless fractions) for Fe atoms in tetrahedral and octahedral positions, respectively. The ratio of recoilless fractions $f\prime_{T_d}/f\prime_{O_h}$ was assumed to be 0.98 and 0.94 for 78 and 296 K, respectively [66]. Since the ratio of ions of different charges in octahedral positions determines the average degree of oxidation of iron atoms, this affects the isomeric shift observed in the Mössbauer spectra [67]. It can be shown that the nonstoichiometry parameter (δ) of magnetite ($Fe_{3-\delta}O_4$) is related to the area of partial spectra in octahedral positions (S_{O_h}) and the corresponding isomeric shifts (δ_{O_h}) by the following expression [68,69]

$$\delta = \frac{\Sigma(\delta_2 - 3\delta_{O_h} + 2\delta_3)S_{O_h} + (\delta_2 - \delta_3)S_{T_d}}{\Sigma(3\delta_2 - \delta_{O_h} - 2\delta_3)S_{O_h} + 3(\delta_2 - \delta_3)S_{T_d}}, \quad (2)$$

where δ_2 = 1.33 ± 0.09 (or 1.16 ± 0.06) mm/s and δ_3 = 0.49 ± 0.04 (or 0.37 ± 0.04) mm/s are isomeric shifts for Fe^{2+} and Fe^{3+} ions at 78 (or 296) K in an octahedral oxygen environment [67], S_{T_d} is the relative area of the subspectrum in the tetrahedral position. S_{T_d} and S_{O_h} were calculated from the experimental spectra taking into account the above-mentioned $f\prime_{T_d}/f\prime_{O_h}$ ratio. The calculations performed according to Equation (2) using the data listed in Table 3 allow us to write the composition of ferromagnetic iron-containing particles as $Fe_{2.782(11)}O_4$ and $Fe_{2.777(5)}O_4$ for 296 and 78 K, respectively. Thus, the Fe@ZSM-5 sample should be considered as deeply oxidized magnetite.

The parameter α of the relaxation model for the sample Fe@ZSM-5 at 296 and 78 K was 3.81(11) and 10.95(25), respectively. This parameter is equal to the ratio of the anisotropy energy of the particle to the thermal energy:

$$\alpha = \frac{KV}{k_B T}, \quad (3)$$

where K is the magnetic anisotropy constant, V is the volume of the magnetic domain, k_B is the Boltzmann constant, and T is the temperature. Let us assume that K does not depend on temperature, but is an additive function depending on the composition of the material:

$$K = K(\gamma\text{-}Fe_2O_3) + X \cdot [K(Fe_3O_4) - K(\gamma\text{-}Fe_2O_3)], \quad (4)$$

where $K(Fe_3O_4) = 1.35 \times 10^4$ J/m^3 [70] and $K(\gamma\text{-}Fe_2O_3) = 4.7 \times 10^3$ J/m^3 [71] constants of magnetic anisotropy for pure iron oxides, and X is the formal mole fraction of magnetite in the material, which is related to the non-stoichiometry parameter δ_2 from Equation (2) by the following expression [62]:

$$X = \frac{1 - 3\delta}{1 + \delta}. \quad (5)$$

Then, expressing the particle volume V from Equation (3), we can estimate the size of the magnetic domains, for example, using a simplified model of spherical-shaped particles. The magnetic domain sizes calculated in this way for the Fe@ZSM-5 sample were 16.04(20) and 14.69(9) nm for 296 and 78 K, respectively. The reason for the apparent

decrease in the detected particle sizes with decreasing temperature is the additional consideration of small particles that were paramagnetic at room temperature. This estimation suggests that the magnetic nanoparticles are formed on the zeolite surface.

The experimental ^{57}Fe Mössbauer spectra of Fe@ZSM-5_0.2 and Fe@ZSM-5_0.4 recorded at 78 and 296 K consist of well-resolved symmetric quadrupole doublets (Figure 6), whose intensity decreases significantly with increasing temperature. They can be fitted by a superposition of two (or three in the case of the sample Fe@ZSM-5_0.2 at 78 K) nested doublets with similar values of isomeric shifts (see Figure 6, Table 5). The values of isomeric shifts for the doublets of all samples correspond to Fe^{3+} ions in an octahedral oxygen environment [67] and are consistent with the literature data for its oxohydroxo compounds [72,73]. Based on the conditions of sample synthesis, it can be assumed that the spectra under consideration correspond to nanoscale particles of iron oxo- or oxohydroxo compounds in a superparamagnetic state with a blocking temperature significantly lower than the boiling point of nitrogen [61,74]. The low blocking temperature is indicated by the absence of temperature dependence of such hyperfine parameters as the quadrupole splitting and the resonance linewidths. The only exception is the spectrum at 78 K of the sample Fe@ZSM-5_0.2, for which it is necessary to introduce into the model an additional doublet with high values of quadrupole splitting and linewidth (Table 5). This doublet formally describes the incipient magnetic ordering with decreasing temperature.

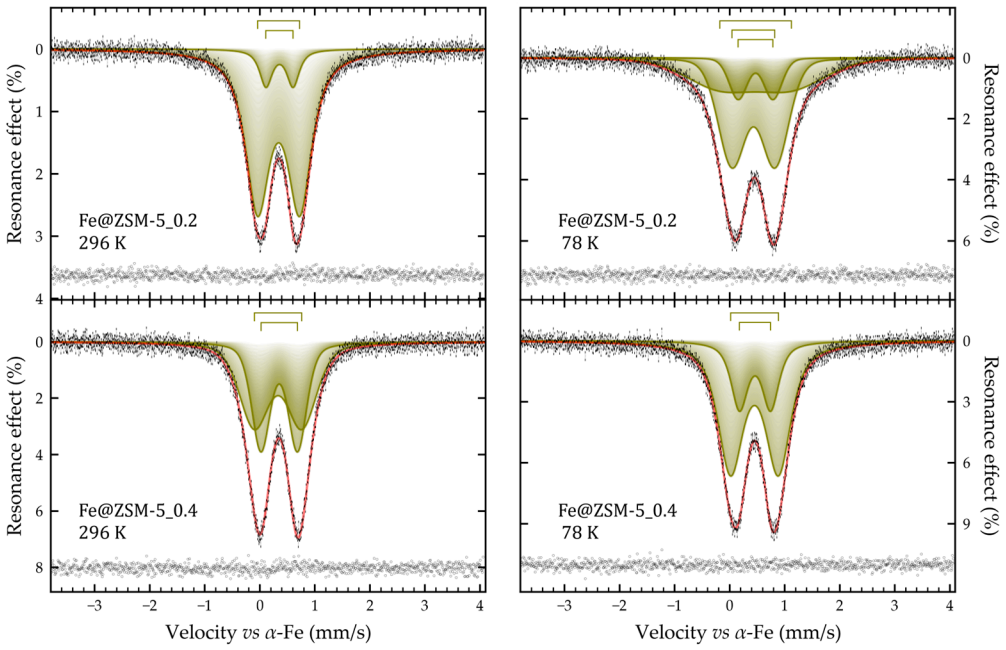


Figure 6. Mössbauer spectra of the Fe@ZSM-5_0.2 (**top**) and Fe@ZSM-5_0.4 (**bottom**) samples obtained at 296 K (**a**) and 78 K (**b**). The size of the dashes corresponds to the error of the experimental points; the result of subtracting the model from the experimental spectrum is presented at the bottom of the figures.

Thus, based on the data obtained, it can be stated that all composite samples contain nanoscale iron- based clusters in the superparamagnetic state, but with markedly different blocking temperatures. Moreover, if for the Fe@ZSM-5 sample, the blocking temperature is higher than room temperature, then for Fe@ZSM-5_0.2 and Fe@ZSM-5_0.4 it is much lower than 78 K, and for and Fe@ZSM-5_0.4 this temperature is the lowest.

Indeed, when all samples are cooled to 5 K, their Mössbauer spectra become similar to each other and represent a superposition of Zeeman sextets (Figure 5). At the same

time, despite the low temperature of spectral registration, their profile remains distorted by relaxation phenomena. The low-temperature spectrum of the Fe@ZSM-5 sample can be satisfactorily described by superposition of only four relaxation sextets (similar to the one described above), with associated relaxation parameters (Table 5). The presence of low-intensity resonance absorbances in the range of −6.5 and −3.0 mm/s on the spectrum profile (Figure 7a) is due to Fe^{2+} in octahedral positions, and is typical for low-temperature magnetite spectra [65,75,76]. In contrast to the described above spectrum of the Fe@ZSM-5 sample on the low-temperature experimental Mössbauer spectra of samples Fe@ZSM-5_0.2 and Fe@ZSM-5_0.4 these absorptions are not observed (Figure 7b,c). However, this may be due to the significantly larger width of the resonance lines for the discussed spectra. The spectra of these two samples can be satisfactorily described within the framework of a model as a superposition of three relaxation sextets (as indicated above), with associated relaxation parameters (Table 5). The calculated hyperfine parameters, such as isomeric shift and quadrupole shift for these samples vary little within the limits of experimental error, which indicates the uniform nature of iron-containing species. However, the widths of the resonance lines and the hyperfine magnetic fields of the sextets for the sample Fe@ZSM-5_0.4 differ markedly from similar parameters for the sample Fe@ZSM-5_0.2 (Table 5): the widths are larger, and the magnitudes of the magnetic splits are smaller. The reason for this phenomenon is the significantly smaller size of the magnetic domains for the sample Fe@ZSM-5_0.4 compared to the Fe@ZSM-5_0.2 sample. Similar observations can be made by comparing the corresponding parameters of these two samples with Fe@ZSM-5: the Fe@ZSM-5 sample differs somewhat in structure (at least in greater order) and in the large size of the magnetic domains (crystallites).

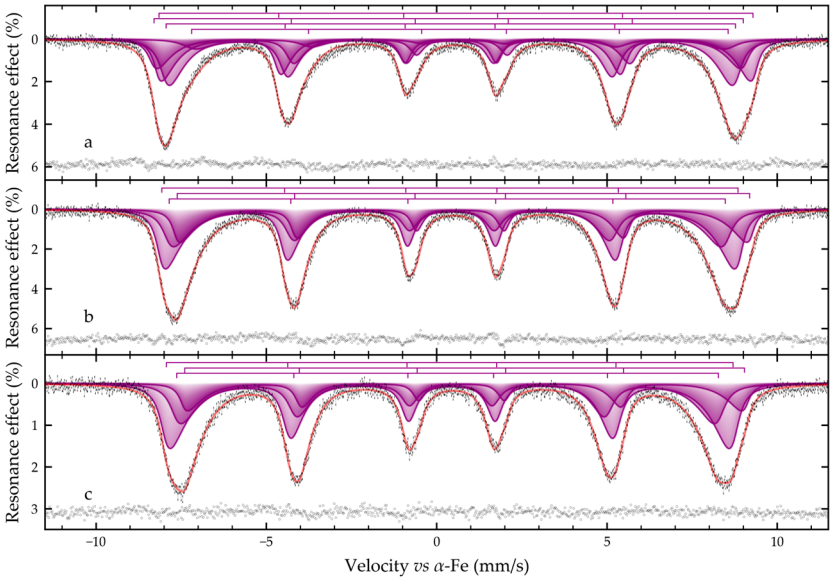


Figure 7. Mössbauer spectra of the (**a**) Fe@ZSM, (**b**) Fe@ZSM-5_0.2 and (**c**) Fe@ZSM-5_0.4 samples obtained at 5 K. The size of the dashes corresponds to the error of the experimental points; the result of subtracting the model from the experimental spectrum is presented at the bottom of the figures.

2.6. UV-Vis Diffuse Reflectance Spectroscopy Studies

The optical properties of the prepared composites were characterized by UV-Vis DRS. The spectra of all samples are shown in Figure 8a. They exhibit similar overall profiles, with at least four main absorption bands, centered at approximately 220, 300, 390 and 450–490 nm. Deconvolution of the spectra are shown in Figure S4 (Supplementary Materials).

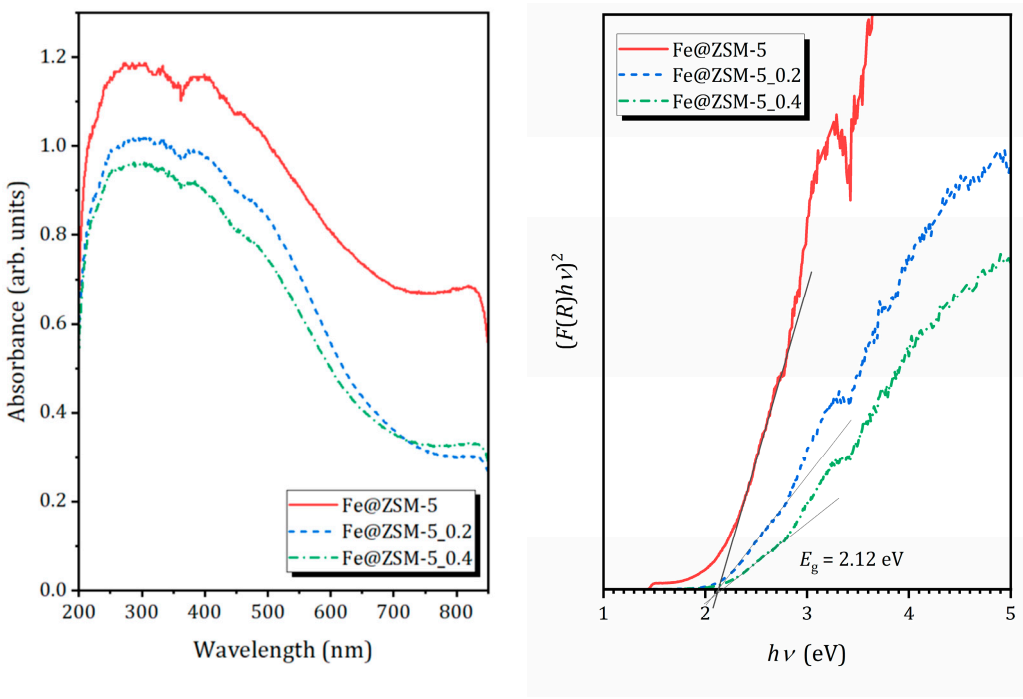


Figure 8. (**a**) UV-vis spectra of the composites; (**b**) $(F(R)h\nu)^2$ versus photon energy for calculation of bandgap.

According to literature reports [77–79] the sub-band at 240 nm can be associated with isolated Fe^{3+} ions in tetrahedral coordination (charge-transfer transitions involving framework oxygen). The broader band centered at about 370 nm is typically assigned to Fe^{3+} ions belonging to small oligonuclear Fe_xO_y clusters; whereas the intense absorption extending from ~450 to 490 nm and beyond is characteristic of larger magnetite Fe_3O_4 nanoparticles. The contribution from Fe^{2+} d–d transitions is expected above 800 nm and thus lies outside the measured range. All these features are clearly observed in the studied composites, with the relative intensities varying between samples in full agreement with Mössbauer spectroscopy results.

In all composites, Fe_xO_y clusters and Fe_3O_4 nanoparticles predominate, while a minor fraction of isolated Fe^{3+} ions are also present. The latter may partially isomorphically substitute Al^{3+} in the zeolite framework. The contribution of crystalline hematite (α-Fe_2O_3) nanoparticles or other bulk iron oxide phases is negligible, consistent with the absence of corresponding reflections in the XRD. Nevertheless, the presence of small amount of various iron-containing nanospecies likely causes partial blockage of the MFI micropores, contributing to the observed reduction in specific surface area.

Band gap energies (E_g), were determined from the transformed diffuse reflectance spectra of the studied composites using the Kubelka–Munk function. The data were plotted as $(F(R)h\nu)^2 = f(h\nu)$, where $F(R) = (1 - R)^2/2R$ is the Kubelka–Munk expression of a reflection coefficient R. The direct bandgap value E_g was estimated from the point of intersection of the linear fit of the Kubelka–Munk graphs with abscise axis [80]. As can be seen from Figure 8b, all the samples show the same energy bandgap of 2.12 eV. This value confirms that these materials are photoactive not only under ultraviolet irradiation but also throughout a significant portion of the visible spectrum, making them promising for solar-driven photocatalytic applications.

3. Materials and Methods

3.1. Synthesis

3.1.1. Preparation of Mesoporous ZSM-5 Matrices

NH_4-ZSM-5 zeolite (MFI framework type, nominal Si/Al = 15, product CBV 3024E) supplied by Zeolyst International (Kansas City, KS, USA) was used as the parent material. Mesoporous ZSM-5 matrices were prepared by alkaline treatment (desilication) of the parent zeolite in aqueous NaOH solution (>99.0%, supplied by Vekton, Saint Petersburg, Russia). In a typical procedure, the zeolite was suspended in 0.2 or 0.4 M NaOH solution and stirred (350 rpm) at 65 °C for 120 min. The suspension was then centrifuged (10–15 min), washed repeatedly with distilled water until the washings reached neutral pH, and dried overnight at 100 °C. The resulting materials are denoted as ZSM-5_0.2 and ZSM-5_0.4, where the number indicates the concentration of NaOH used for desilication.

3.1.2. Synthesis of Magnetite–Zeolite Composites

Magnetite–zeolite composites were prepared by co-precipitation of Fe^{2+} and Fe^{3+} ions in the presence of the zeolite matrix under oxygen-free conditions. The following reagents were used: $FeCl_3 \cdot 6H_2O$ (≥99%), $FeSO_4 \cdot 7H_2O$ (≥99%), NaOH (reagent grade), CH_2Cl_2 (≥99.8%), and deionized water. All chemicals are supplied by Vekton (Saint Petersburg, Russia).

In a typical synthesis, 0.50 g of zeolite (parent ZSM-5 or mesoporous ZSM-5_0.2/ZSM-5_0.4) was dispersed in 10 mL of deionized water previously deoxygenated by bubbling with argon for at least 30 min. Subsequently, 0.30 g of $FeCl_3 \cdot 6H_2O$ (corresponding to $[Fe^{3+}]$ = 0.111 M in the final reaction mixture) and 0.24 g of $FeSO_4 \cdot 7H_2O$ ($[Fe^{2+}]$ = 0.086 M in the final reaction mixture) were added. The suspension was stirred vigorously, evacuated using a water-jet pump, and maintained under vacuum with continuous stirring for 15 min to promote impregnation of iron species into the zeolite pores. Thereafter, a deoxygenated 1 M NaOH solution was added dropwise until the pH reached 10–12 (monitored with universal indicator paper). The mixture was then stirred vigorously for 1 h at room temperature under an argon atmosphere. All solutions and water used throughout the synthesis were pre-degassed with argon to prevent premature oxidation of Fe^{2+}.

The resulting dark precipitate was collected by filtration, washed thoroughly with deionized water followed by methylene chloride to remove residual chloride and sulfate ions, and dried under reduced pressure on a rotary evaporator (bath temperature 60 °C, 40 mbar) for 1 h. The obtained composites were stored under argon in sealed vials to prevent oxidation of the magnetite phase.

The samples are designated as Fe@ZSM-5 (iron supported on parent microporous ZSM-5), Fe@ZSM-5_0.2, and Fe@ZSM-5_0.4 (iron supported on matrices treated with 0.2 M and 0.4 M NaOH, respectively).

3.2. Characterization

XRD patterns were recorded on a Rigaku Miniflex II benchtop diffractometer (Rigaku Corporation, Tokyo, Japan) using Cu K_α radiation (λ = 1.5406 Å). Data were collected in the 2θ range of 3–60° with a step width of 0.02° and a scan rate of 2° min^{-1}. Elemental composition was determined by EDXRF under vacuum using a Shimadzu EDX 800 HS apparatus (Shimadzu Corporation, Kyoto, Japan). SEM-EDX studies were performed using a Zeiss Merlin field-emission scanning electron microscope (Carl Zeiss Microscopy GmbH, Oberkochen, Germany) equipped with an Oxford Instruments INCAx-act EDX console.

XPS spectra were obtained using a Thermo Fisher Scientific Escalab 250Xi spectrometer (Thermo Fisher Scientific, Waltham, MA, USA) with non-monochromatic Al Kα radiation (photon energy 1486.6 eV).

N_2 adsorption/desorption isotherms were obtained at 77 K using the Quadrasorb SI 2SI-MP-20 equipment (Quantachrome Instruments, Boynton Beach, FL, USA). Before analysis, the samples were outgassed under vacuum in a FLOVAC Degasser FVD-3 degasser (Anton Paar GmbH, Graz, Austria) for 3 h at 300 °C.

Magnetic properties were measured at 300 K using a Lake Shore Cryotronics Inc. (Westerville, Ohio, USA) Model 7410 vibrating-sample magnetometer (VSM). Hysteresis loops were recorded by sweeping the applied magnetic field from −18 to +18 kOe at a frequency of 77 Hz.

Diffuse reflectance UV–Vis spectra (DRS) were recorded on a Persee T8DCS spectrophotometer (Auburn, CA, USA) equipped with an SI19-1 integrating sphere. Spectra were collected over the wavelength range of 190–900 nm using $BaSO_4$ as a reference.

^{57}Fe Mössbauer absorption spectra were measured in transmission geometry with a moving source and triangular velocity reference signals on an express Mössbauer spectrometer MS1104EM (CJSC Kordon, Rostov-on-Don, Russia). Spectra were accumulated at 296(3) K, 77.7(0.3) K and 5.000(3) K using a Cryogen-free closed cycle cryostat for Mössbauer spectroscopy CFPR-221-MESS (LLC Kriogennye Pribory, Moscow, Russia). The source of γ-radiation was ^{57}Co in a matrix of metallic rhodium with an activity of approximately 10 mCi (Cyclotron Co., Ltd., Obninsk, Russia), maintained at room temperature during measurements. Velocity calibration was performed using a standard α-Fe foil absorber. The signal-to-noise ratio of the accumulated spectra did not exceed 2%. High-resolution spectra (1024 channels) were processed and fitted using SpectRelax 4.1 software (Lomonosov Moscow State University, Moscow, Russia) [81]. Values of isomer shifts are reported relative to α-Fe at 296 K.

4. Conclusions

The influence of tunable hierarchical porosity of ZSM-5 zeolite on the composition and properties of iron-containing species formed during the synthesis of magnetite supported on the zeolite matrix has been studied. Magnetite is present in all samples; however, the particle size and stoichiometry are strongly governed by the extent of post-synthetic desilication. The generated mesoporosity in the ZSM-5 matrix plays a decisive role in the nature of the supported iron species: mild alkaline treatment promotes the formation of nanocrystalline, partially oxidized magnetite mainly located on the external surface of the zeolite, whereas strong desilication leads to the formation of ultra-small, highly dispersed Fe(III) oxide/hydroxide clusters confined within mesopores. This structural evolution results in a gradual transition from superparamagnetic behavior at room temperature to paramagnetic, accompanied by a sharp decrease in saturation magnetization.

Despite these differences, all composites exhibit identical optical band gaps of ~2.12 eV, ensuring efficient visible-light harvesting. The obtained materials combine high adsorption capacity and magnetic separability, making the microporous composite (Fe@ZSM-5) particularly promising as a reusable visible-light photocatalyst with excellent mass transfer properties due to the developed mesoporosity.

The present study highlights the important role of controlled mesoporosity generation in the support for tuning the dispersion of the active phase and provides a rational basis for the design of advanced magnetite–zeolite photocatalysts for solar-driven water purification. Thus, the studied composites have great potential for use in additive technologies combining photocatalysis, high kinetics, and magnetic separation. However, further optimization efforts are needed, as increasing porosity (important for transport properties) simultaneously leads to greater dispersion and smaller magnetite particles, thereby reducing magnetic response.

Supplementary Materials: The following supporting information can be downloaded at: https://www.mdpi.com/article/10.3390/molecules31010089/s1, Figure S1: SEM images for the studied composites (on the right) and parent zeolite matrices (on the left); Figure S2: Element distribution maps in the studied Fe@zeolite composites according to SEM-EDX; Figure S3: Magnetization hysteresis loop for studied composites; Figure S4: Decomposition of UV-Vis spectra (on the left); $(F(R)hv)^2$ versus photon energy for calculation of bandgap energies for the studied composites (on the right).

Author Contributions: Conceptualization, I.A.Z., M.G.S. and V.P.; methodology, I.A.Z., D.A.P. and E.G.Z.; validation, D.A.P. and M.G.S.; formal analysis, S.A.K.; investigation, D.A.P., A.S., V.K.K., S.A.K. and S.O.K.; resources, M.G.S.; data curation, D.A.P., A.S., S.A.K., V.K.K. and S.O.K.; writing—original draft preparation, D.A.P., M.G.S. and V.P.; writing—review and editing, D.A.P., M.G.S. and V.P.; visualization, D.A.P. and M.G.S.; project administration, M.G.S.; funding acquisition, M.G.S. All authors have read and agreed to the published version of the manuscript.

Funding: This work was supported by the Russian Federation, represented by the Ministry of Science and Higher Education of Russia, through agreement No. 075-15-2025-661, dated 25 August 2025, and by DGAPA–PAPIIT Grant IG101623 (UNAM).

Institutional Review Board Statement: Not applicable.

Informed Consent Statement: Not applicable.

Data Availability Statement: The original contributions presented in this study are included in the article/Supplementary Materials. Further inquiries can be directed to the corresponding author(s).

Acknowledgments: The authors thank the Research Park of Saint Petersburg State University (Centre for Diagnostics of Functional Materials for Medicine, Pharmacology and Nanoelectronics, Centre for X-ray Diffraction Studies, Centre for Physical Methods of Surface Investigation, Centre for Innovative Technologies of Composite Nanomaterials, Interdisciplinary Resource Centre for Nanotechnology, Centre for Optical and Laser Materials Research) and the Development Program of Lomonosov Moscow State University for the access to the Cryogen-free closed cycle cryostat for Mössbauer spectroscopy CFPR-221-MESS.

Conflicts of Interest: The authors declare no conflicts of interest.

Abbreviations

The following abbreviations are used in this manuscript:

BET	Brunauer–Emmett–Teller (method)
BJH	Barrett–Joyner–Halenda (method)
DRS	Diffuse reflectance spectroscopy
EDX	Energy-dispersive X-ray (spectroscopy)
EDXRF	Energy dispersive X-ray fluorescence spectroscopy
SEM	Scanning electron microscopy
VSM	Vibrating-sample magnetometry
UV–Vis	Ultraviolet–visible spectroscopy
XRD	X-ray diffraction
ZSM-5	Zeolite Socony Mobil-5

References

1. Parangi, T. Heterogeneous Catalysis: An Alternative Approach for Energy and Environment. *Rev. Inorg. Chem.* **2025**, *45*, 831–861. [CrossRef]
2. Čejka, J.; Millini, R.; Opanasenko, M.; Serrano, D.P.; Roth, W.J. Advances and Challenges in Zeolite Synthesis and Catalysis. *Catal. Today* **2020**, *345*, 2–13. [CrossRef]
3. Wang, Z.; Yu, J.; Xu, R. Needs and Trends in Rational Synthesis of Zeolitic Materials. *Chem. Soc. Rev.* **2012**, *41*, 1729–1741. [CrossRef]

4. Yuna, Z. Review of the Natural, Modified, and Synthetic Zeolites for Heavy Metals Removal from Wastewater. *Environ. Eng. Sci.* **2016**, *33*, 443–454. [CrossRef]
5. Baerlocher, C.; McCusker, L.B. Database of Zeolite Structures. Available online: http://www.iza-structure.org/databases/ (accessed on 30 November 2025).
6. Masoumifard, N.; Guillet-Nicolas, R.; Kleitz, F. Synthesis of Engineered Zeolitic Naterials: From Classical Zeolites to Hierarchical Core–Shell Materials. *Adv. Mater.* **2018**, *30*, 1704439. [CrossRef]
7. Radoor, S.; Karayil, J.; Kim, H. Recent Advances in ZSM-5 Zeolite for Multi-Pollutant Removal from Water: A Mini Review. *Microporous Mesoporous Mater.* **2026**, *399*, 113841. [CrossRef]
8. Palčić, A.; Valtchev, V. Analysis and Control of Acid Sites in Zeolites. *Appl. Catal. A Gen.* **2020**, *606*, 117795. [CrossRef]
9. Shelyapina, M.G.; Krylova, E.A.; Mazur, A.S.; Tsyganenko, A.A.; Shergin, Y.V.; Satikova, E.; Petranovskii, V. Active Sites in H-Mordenite Catalysts Probed by NMR and FTIR. *Catalysts* **2022**, *13*, 344. [CrossRef]
10. Kessouri, A.; Boukoussa, B.; Bengueddach, A. Synthesis of Iron-MFI Zeolite and Its Photocatalytic Application for Hydroxylation of Phenol. *Res. Chem. Intermed.* **2017**, *44*, 2475–2487. [CrossRef]
11. Kouadio, K.S.; Tchirioua, E.; Dhainaut, J. Zeolitized Clays and Their Use for the Capture and Photo-Fenton Degradation of Methylene Blue. *Catalysts* **2025**, *15*, 188. [CrossRef]
12. Du, T.; Chao, Y.; Meng, C.; He, Z.; Zhao, Y.; Miao, Z. The Role and Progress of Zeolites in Photocatalytic Materials. *Environ. Res.* **2025**, *268*, 120771. [CrossRef]
13. He, F.; Jeon, W.; Choi, W. Photocatalytic Air Purification Mimicking the Self-Cleaning Process of the Atmosphere. *Nat. Commun.* **2021**, *12*, 10–13. [CrossRef] [PubMed]
14. Hu, G.; Yang, J.; Duan, X.; Farnood, R.; Yang, C.; Yang, J.; Liu, W.; Liu, Q. Recent Developments and Challenges in Zeolite-Based Composite Photocatalysts for Environmental Applications. *Chem. Eng. J.* **2021**, *417*, 129209. [CrossRef]
15. Wang, L.; Wang, W.; Liu, M.; Ge, H.; Zha, W.; Wei, Y.; Fei, E.; Zhang, Z.; Long, J.; Sa, R.; et al. Understanding Structure-Function Relationships in HZSM-5 Zeolite Catalysts for Photocatalytic Oxidation of Isopropyl Alcohol. *J. Catal.* **2019**, *377*, 322–331. [CrossRef]
16. Hashimoto, S. Zeolite Photochemistry: Impact of Zeolites on Photochemistry and Feedback from Photochemistry to Zeolite Science. *J. Photochem. Photobiol. C Photochem. Rev.* **2003**, *4*, 19–49. [CrossRef]
17. Shelyapina, M.G.; Yocupicio-gaxiola, R.I.; Valkovsky, G.A.; Petranovskii, V. TiO_2 Immobilized on 2D Mordenite: Effect of Hydrolysis Conditions on Structural, Textural, and Optical Characteristics of the Nanocomposites. *Beilstein J. Nanotechnol.* **2025**, *16*, 128–140. [CrossRef]
18. Zong, X.; Wang, L. Ion-Exchangeable Semiconductor Materials for Visible Light-Induced Photocatalysis. *J. Photochem. Photobiol. C Photochem. Rev.* **2014**, *18*, 32–49. [CrossRef]
19. Valtchev, V.; Majano, G.; Mintova, S.; Pérez-Ramírez, J. Tailored Crystalline Microporous Materials by Post-Synthesis Modification. *Chem. Soc. Rev.* **2013**, *42*, 263–290. [CrossRef] [PubMed]
20. Petranovskii, V.; Chaves-Rivas, F.; Hernandez Espinoza, M.A.; Pestryakov, A.; Kolobova, E. Potential Uses of Natural Zeolites for the Development of New Materials: Short Review. *MATEC Web Conf.* **2016**, *85*, 01014. [CrossRef]
21. Znad, H.; Abbas, K.; Hena, S.; Awual, M.R. Synthesis a Novel Multilamellar Mesoporous TiO_2/ZSM-5 for Photo-Catalytic Degradation of Methyl Orange Dye in Aqueous Media. *J. Environ. Chem. Eng.* **2018**, *6*, 218–227. [CrossRef]
22. Kornas, A.; Mlekodaj, K.; Tabor, E. Nature and Redox Properties of Iron Sites in Zeolites Revealed by Mössbauer Spectroscopy. *Chempluschem* **2024**, *89*, e202300543. [CrossRef] [PubMed]
23. Zhang, J.; Tang, X.; Yi, H.; Yu, Q.; Zhang, Y.; Wei, J.; Yuan, Y. Synthesis, Characterization and Application of Fe-Zeolite: A Review. *Appl. Catal. A Gen.* **2022**, *630*, 118467. [CrossRef]
24. Bernal-Villamil, I.; Gallego, S. Electronic Phase Transitions in Ultrathin Magnetite Films. *J. Phys. Condens. Matter* **2015**, *27*, 293202. [CrossRef]
25. Huang, J.; Jones, A.; Waite, T.D.; Chen, Y.; Huang, X.; Rosso, K.M.; Kappler, A.; Mansor, M.; Tratnyek, P.G.; Zhang, H. Fe(II) Redox Chemistry in the Environment. *Chem. Rev.* **2021**, *121*, 8161–8233. [CrossRef]
26. Robinson, T.C.; Latta, D.E.; Leddy, J.; Scherer, M.M. Redox Potentials of Magnetite Suspensions under Reducing Conditions. *Environ. Sci. Technol.* **2022**, *56*, 17454–17461. [CrossRef] [PubMed]
27. Pereira, M.C.; Oliveira, L.C.A.; Murad, E. Iron Oxide Catalysts: Fenton and Fentonlike Reactions—A Review. *Clay Miner.* **2012**, *47*, 285–302. [CrossRef]
28. Shah, S.I.A.; Ahmad, W.; Anwar, M.; Shah, R.; Khan, J.A.; Shah, N.S.; Al-Anazi, A.; Han, C. Synthesis, Properties, and Applications of Fe_3O_4 and Fe_3O_4-Based Nanocomposites: A Review. *Appl. Catal. O Open* **2025**, *203*, 207049. [CrossRef]
29. Karim, A.V.; Krishnan, S.; Shriwastav, A. An Overview of Heterogeneous Photocatalysis for the Degradation of Organic Compounds: A Special Emphasis on Photocorrosion and Reusability. *J. Indian Chem. Soc.* **2022**, *99*, 100480. [CrossRef]
30. Qin, F.; Xia, Y.; Yang, D.; Xiao, T.; Zhu, X.; Feng, W. Enhanced Photocatalytic Activity of G-C_3N_4/Bi_2WO_6 Heterojunction via Z-Scheme Charge-Transfer Mechanism. *J. Mol. Struct.* **2024**, *1316*, 139023. [CrossRef]

31. Qin, F.; Luo, Y.; Yu, Q.; Cheng, J.; Qin, Q.; Zhu, X.; Feng, W. Enhanced Charge Transfer and Photocatalytic Activity of $BiOBr/Bi_2WO_6$ p-n Heterojunctions. *J. Mol. Struct.* **2024**, *1304*, 137719. [CrossRef]
32. Tang, D.; Pal, M.; Meng, T.; Mao, D.; Xue, Z. Synthesis and Applications of Magnetic Zeolites: A Comprehensive Review. *J. Supercond. Nov. Magn.* **2025**, *38*, 146. [CrossRef]
33. Bisaria, K.; Sinha, S.; Singh, R.; Iqbal, H.M.N. Recent Advances in Structural Modifications of Photo-Catalysts for Organic Pollutants Degradation—A Comprehensive Review. *Chemosphere* **2021**, *284*, 131263. [CrossRef] [PubMed]
34. Du, T.; Zheng, S.; Zhang, Y.; Zhang, Y.; Wang, B.; Song, W.; Meng, C.; Zhao, Y.; Miao, Z. Recent Progress in Zeolite-Based Photocatalysts: Strategies for Improving Photocatalytic Performance. *J. Alloys Compd.* **2025**, *1035*, 181573. [CrossRef]
35. Sharma, V.; Javed, B.; Byrne, H.; Curtin, J.; Tian, F. Zeolites as Carriers of Nano-Fertilizers: From Structures and Principles to Prospects and Challenges. *Appl. Nano* **2022**, *3*, 163–186. [CrossRef]
36. Zhou, H.; Ge, M.; Zhao, H.; Wu, S.; Li, M.; Su, Y. Selective Catalytic Reduction of Nitric Oxide with Propylene over Fe/Beta Catalysts under Lean-Burn Conditions. *Catalysts* **2019**, *9*, 205. [CrossRef]
37. Jiang, H.; Xu, L.; Meng, Q.; Feng, X.; Wang, J.; Li, Y.; Li, J. Construction of Hierarchical Fe-MFI Nanosheets with Enhanced Fenton-like Degradation Performance. *Molecules* **2025**, *30*, 430. [CrossRef]
38. Diallo, M.M.; Laforge, S.; Pouilloux, Y.; Mijoin, J. Influence of the Preparation Procedure and Crystallite Size of Fe-MFI Zeolites in the Oxidehydration of Glycerol to Acrolein and Acrylic Acid. *Catal. Commun.* **2019**, *126*, 21–25. [CrossRef]
39. Shelyapina, M.G.; Gurgul, J.; Łątka, K.; Bogdanov, D.; Kotolevich, Y.; Petranovskii, V.; Fuentes, S.; Sánchez-López, P.; Bogdanov, D.; Kotolevich, Y.; et al. Mechanism of Formation of Framework Fe^{3+} in Bimetallic Ag-Fe Mordenites—Effective Catalytic Centers for DeNOx Reaction. *Microporous Mesoporous Mater.* **2019**, *299*, 109841. [CrossRef]
40. Zvereva, I.A.; Samadov, A.; Kurnosenko, S.A.; Kirichenko, S.O.; Shelyapina, M.G.; Petranovskii, V. Effect of Mesoporosity on Structural, Textural, and Optical Characteristics of Fe(III) Ion-Exchanged ZSM-5 Zeolites. *Molecules* **2026**, *31*, 23. [CrossRef]
41. Reyes Villegas, V.A.; De León Ramirez, J.I.; Pérez-Cabrera, L.; Pérez-Sicairos, S.; Chávez-Méndez, J.R.; Petranovskii, V. Analysis of Catalytic Sites in FeY Zeolite Prepared by Sono-Assisted Exchange of Iron (II) Ions. *Microporous Mesoporous Mater.* **2024**, *380*, 113306. [CrossRef]
42. Ko, Y.S.; Jang, H.T.; Ahn, W.S. Hydrothermal Synthesis and Characterization of Fe(III)-Substituted Mordenites. *Korean J. Chem. Eng.* **2008**, *25*, 1286–1291. [CrossRef]
43. Wu, P.; Komatsu, T.; Yashima, T. Isomorphous Substitution of Fe^{3+} in the Framework of Aluminosilicate Mordenite by Hydrothermal Synthesis. *Microporous Mesoporous Mater.* **1998**, *20*, 139–147. [CrossRef]
44. Möller, K.; Bein, T. Mesoporosity—A New Dimension for Zeolites. *Chem. Soc. Rev.* **2013**, *42*, 3689–3707. [CrossRef]
45. Oliveira, D.S.; Lima, R.B.; Pergher, S.B.C.; Caldeira, V.P.S. Hierarchical Zeolite Synthesis by Alkaline Treatment: Advantages and Applications. *Catalysts* **2023**, *13*, 316. [CrossRef]
46. Lago, C.D.; Decolatti, H.P.; Tonutti, L.G.; Dalla Costa, B.O.; Querini, C.A. Gas Phase Glycerol Dehydration over H-ZSM-5 Zeolite Modified by Alkaline Treatment with Na_2CO_3. *J. Catal.* **2018**, *366*, 16–27. [CrossRef]
47. Milina, M.; Mitchell, S.; Crivelli, P.; Cooke, D.; Pérez-Ramírez, J. Mesopore Quality Determines the Lifetime of Hierarchically Structured Zeolite Catalysts. *Nat. Commun.* **2014**, *5*, 3922. [CrossRef]
48. Al-Ani, A.; Darton, R.J.; Sneddon, S.; Zholobenko, V. Nanostructured Zeolites: The Introduction of Intracrystalline Mesoporosity in Basic Faujasite-Type Catalysts. *ACS Appl. Nano Mater.* **2018**, *1*, 310–318. [CrossRef]
49. Zhang, R.; Xu, S.; Raja, D.; Khusni, N.B.; Liu, J.; Zhang, J.; Abdulridha, S.; Xiang, H.; Jiang, S.; Guan, Y.; et al. On the Effect of Mesoporosity of FAU Y Zeolites in the Liquid-Phase Catalysis. *Microporous Mesoporous Mater.* **2019**, *278*, 297–306. [CrossRef]
50. Hernández-Giménez, A.M.; Heracleous, E.; Pachatouridou, E.; Horvat, A.; Hernando, H.; Serrano, D.P.; Lappas, A.A.; Bruijnincx, P.C.A.; Weckhuysen, B.M. Effect of Mesoporosity, Acidity and Crystal Size of Zeolite ZSM-5 on Catalytic Performance during the Ex-Situ Catalytic Past Pyrolysis of Biomass. *ChemCatChem* **2021**, *13*, 1207–1219. [CrossRef]
51. Shelyapina, M.G.; Yocupicio-Gaxiola, R.I.; Zhelezniak, I.V.; Chislov, M.V.; Antúnez-García, J.; Murrieta-Rico, F.N.; Galván, D.H.; Petranovskii, V.; Fuentes-Moyado, S. Local Structures of Two-Dimensional Zeolites—Mordenite and ZSM-5—Probed by Multinuclear NMR. *Molecules* **2020**, *25*, 4678. [CrossRef]
52. García-Martínez, L.; Li, K. (Eds.) *Mesoporous Zeolites: Preparation, Characterization and Applications*; Wiley-VCH Verlag GmbH & Co. KGaA: Weinheim, Germany, 2015; ISBN 978-3-527-33574-9.
53. Mitchell, S.; Pinar, A.B.; Kenvin, J.; Crivelli, P.; Kärger, J.; Pérez-Ramírez, J.; Pe, J. Structural Analysis of Hierarchically Organized Zeolites. *Nat. Commun.* **2015**, *6*, 8633. [CrossRef] [PubMed]
54. Liu, Q.; He, P.; Qian, X.; Fei, Z.; Zhang, Z.; Chen, X.; Tang, J.; Cui, M.; Qiao, X.; Shi, Y. Enhanced CO_2 Adsorption Performance on Hierarchical Porous ZSM-5 Zeolite. *Energy Fuels* **2017**, *31*, 13933–13941. [CrossRef]
55. Shelyapina, M.G.; Nefedov, D.Y.; Antonenko, A.O.; Valkovskiy, G.A.; Yocupicio-gaxiola, R.I.; Petranovskii, V. Nanoconfined Water in Pillared Zeolites Probed by ^1H Nuclear Magnetic Resonance. *Int. J. Mol. Sci.* **2023**, *24*, 15898. [CrossRef]

56. Na, K.; Park, W.; Seo, Y.; Ryoo, R. Disordered Assembly of MFI Zeolite Nanosheets with a Large Volume of Intersheet Mesopores. *Chem. Mater.* **2011**, *23*, 1273–1279. [CrossRef]
57. Gaspar, A.B. Synthesis of a Magnetic Fe_3O_4/RGO Composite for the Rapid Photo-Fenton Discoloration of Indigo Carmine Dye. *Top. Catal.* **2020**, *63*, 1017–1029. [CrossRef]
58. Alsulami, Q.A.; Rajeh, A.; Mannaa, M.A.; Albukhari, S.M. One—Step Preparation of RGO/Fe_3O_4–$FeVO_4$ Nanocomposites as Highly Effective Photocatalysts under Natural Sunlight Illumination. *Sci. Rep.* **2022**, *12*, 6565. [CrossRef]
59. Cao, J.; Sun, Q.; Wang, P.; Shen, J.; Dai, X. Synthesize and Characterize of Fe_3O_4/Zeolite 4A Magnetic Nanocomposite. *J. Dispers. Sci. Technol.* **2020**, *43*, 517–525. [CrossRef]
60. Pankratov, D.A.; Anuchina, M.M.; Spiridonov, F.M.; Krivtsov, G.G. $Fe_{3-\delta}O_4$ Nanoparticles Synthesized in the Presence of Natural Polyelectrolytes. *Crystallogr. Rep.* **2020**, *65*, 393–397. [CrossRef]
61. Chernavskiy, P.A.; Novakova, A.A.; Pankina, G.V.; Pankratov, D.A.; Panfilov, S.I.; Petrovskaya, G.A. Synthesis and Characterization of Hematite, Magnetite and Maghemite Supported on Silica Gel. *Magnetochemistry* **2023**, *9*, 228. [CrossRef]
62. Bondarenko, L.S.; Pankratov, D.A.; Dzeranov, A.A.; Dzhardimalieva, G.I.; Streltsova, A.N.; Zarrelli, M.; Kydralieva, K.A. A Simple Method for Quantification of Nonstoichiometric Magnetite Nanoparticles Using Conventional X-Ray Diffraction Technique. *Mendeleev Commun.* **2022**, *32*, 642–644. [CrossRef]
63. Pankratov, D.A.; Anuchina, M.M. Nature-Inspired Synthesis of Magnetic Non-Stoichiometric Fe_3O_4 Nanoparticles by Oxidative in Situ Method in a Humic Medium. *Mater. Chem. Phys.* **2019**, *231*, 216–224. [CrossRef]
64. Klygach, D.S.; Vakhitov, M.G.; Pankratov, D.A.; Zherebtsov, D.A.; Tolstoguzov, D.S.; Raddaoui, Z.; El Kossi, S.; Dhahri, J.; Vinnik, D.A.; Trukhanov, A.V. MCC: Specific of Preparation, Correlation of the Phase Composition and Electrodynamic Properties. *J. Magn. Magn. Mater.* **2021**, *526*, 167694. [CrossRef]
65. Bondarenko, L.; Baimuratova, R.; Reindl, M.; Zach, V.; Dzeranov, A.; Pankratov, D.; Kydralieva, K.; Dzhardimalieva, G.; Kolb, D.; Wagner, F.E.; et al. Dramatic Change in the Properties of Magnetite-Modified MOF Particles Depending on the Synthesis Approach. *Heliyon* **2024**, *10*, e27640. [CrossRef] [PubMed]
66. Sawatzky, G.A.; Van Der Woude, F.; Morrish, A.H. Recoilless-Fraction Ratios for Fe^{57} in Octahedral and Tetrahedral Sites of a Spinel and a Garnet. *Phys. Rev.* **1969**, *183*, 383–386. [CrossRef]
67. Pankratov, D.A. Mössbauer Study of Oxo Derivatives of Iron in the Fe_2O_3-Na_2O_2 System. *Inorg. Mater.* **2014**, *50*, 82–89. [CrossRef]
68. Dzeranov, A.; Bondarenko, L.; Pankratov, D.; Dzhardimalieva, G.; Jorobekova, S.; Saman, D.; Kydralieva, K. Impact of Silica-Modification and Oxidation on the Crystal Structure of Magnetite Nanoparticles. *Magnetochemistry* **2023**, *9*, 18. [CrossRef]
69. Shoppert, A.; Valeev, D.; Diallo, M.M.; Loginova, I.; Beavogui, M.C.; Rakhmonov, A.; Ovchenkov, Y.; Pankratov, D. High-Iron Bauxite Residue (Red Mud) Valorization Using Hydrochemical Conversion of Goethite to Magnetite. *Materials* **2022**, *15*, 8423. [CrossRef]
70. Goya, G.F.; Berquó, T.S.; Fonseca, F.C.; Morales, M.P. Static and Dynamic Magnetic Properties of Spherical Magnetite Nanoparticles. *J. Appl. Phys.* **2003**, *94*, 3520–3528. [CrossRef]
71. Martínez, B.; Roig, A.; Obradors, X.; Molins, E.; Rouanet, A.; Monty, C. Magnetic Properties of γ-Fe_2O_3 Nanoparticles Obtained by Vaporization Condensation in a Solar Furnace. *J. Appl. Phys.* **1996**, *79*, 2580–2586. [CrossRef]
72. Severin, A.V.; Pankratov, D.A. Synthesis of Nanohydroxyapatite in the Presence of Iron(III) Ions. *Russ. J. Inorg. Chem.* **2016**, *61*, 265–272. [CrossRef]
73. Zhirkova, A.M.; Zykova, M.V.; Buyko, E.E.; Ushakova, K.A.; Ivanov, V.V.; Pankratov, D.A.; Udut, E.V.; Azarkina, L.A.; Bashirov, S.R.; Plotnikov, E.V.; et al. Humics-Functionalized Iron(III) Oxyhydroxides as Promising Nanoferrotherapeutics: Synthesis, Characterization, and Efficacy in Iron Delivery. *Nanomaterials* **2025**, *15*, 1400. [CrossRef] [PubMed]
74. Dzeranov, A.; Bondarenko, L.; Pankratov, D.; Prokof'ev, M.; Dzhardimalieva, G.; Jorobekova, S.; Tropskaya, N.; Telegina, L.; Kydralieva, K. Iron Oxides Nanoparticles as Components of Ferroptosis-Inducing Systems: Screening of Potential Candidates. *Magnetochemistry* **2023**, *9*, 3. [CrossRef]
75. Berry, F.J.; Skinner, S.; Thomas, M.F. ^{57}Fe Mössbauer Spectroscopic Examination of a Single Crystal of Fe_3O_4. *J. Phys. Condens. Matter* **1998**, *10*, 215. [CrossRef]
76. Hah, H.Y.; Gray, S.; Johnson, C.E.; Johnson, J.A.; Kolesnichenko, V.; Kucheryavy, P.; Goloverda, G. Mössbauer Spectroscopy of Superparamagnetic Fe_3O_4 Nanoparticles. *J. Magn. Magn. Mater.* **2021**, *539*, 168382. [CrossRef]
77. Nedyalkova, R.; Shwan, S.; Skoglundh, M.; Olsson, L. Improved Low-Temperature SCR Activity for Fe-BEA Catalysts by H_2 -Pretreatment. *Appl. Catal. B Environ.* **2013**, *138–139*, 373–380. [CrossRef]
78. Chen, J.; Peng, G.; Zheng, W.; Zhang, W.; Guo, L.; Wu, X. Excellent Performance of One-Pot Synthesized Fe-Containing MCM-22 Zeolites for the Selective Catalytic Reduction of NO_x with NH_3. *Catal. Sci. Technol.* **2020**, *10*, 6583–6598. [CrossRef]
79. Pérez-Ramírez, J. Active Iron Sites Associated with the Reaction Mechanism of N_2O Conversions over Steam-Activated FeMFI Zeolites. *J. Catal.* **2004**, *227*, 512–522. [CrossRef]

80. Makuła, P.; Pacia, M.; Macyk, W. How to Correctly Determine the Band Gap Energy of Modified Semiconductor Photocatalysts Based on UV−Vis Spectra. *J. Phys. Chem. Lett.* **2018**, *9*, 6814–6817. [CrossRef]
81. Matsnev, M.E.; Rusakov, V.S. SpectrRelax: An Application for Mössbauer Spectra Modeling and Fitting. *AIP Conf. Proc.* **2012**, *1489*, 178–185. [CrossRef]

Disclaimer/Publisher's Note: The statements, opinions and data contained in all publications are solely those of the individual author(s) and contributor(s) and not of MDPI and/or the editor(s). MDPI and/or the editor(s) disclaim responsibility for any injury to people or property resulting from any ideas, methods, instructions or products referred to in the content.